Research

CrossMark
click for updates

Author for correspondence:
S. Residori
e-mail: stefania.residori@inln.cnrs.fr

Light–matter interaction induces a single positive vortex with swirling arms

R. Barboza[1,2], U. Bortolozzo[2], M. G. Clerc[1],
S. Residori[2,3] and E. Vidal-Henriquez[1]

[1]Departamento de Física, FCFM, Universidad de Chile, Casilla 487-3, Santiago, Chile
[2]INLN, Université de Nice-Sophia Antipolis, CNRS, 1361 Route des Lucioles, 06560 Valbonne, France
[3]University of Verona, Department of Computer Science, Strada Le Grazie 15, 37134 Verona, Italy

Homeotropic nematic liquid crystal cells with a photosensitive wall and negative dielectric anisotropy exhibit, under the influence of local illumination, stable vortexes with swirling arms that are trapped at the illuminated area. Close to the Fréedericksz transition an amplitude equation is derived, which allows us to understand the origin of the induced vortex and the competition between the illuminating profile and the elastic anisotropy generating the swirling of the arms.

1. Introduction

Motivated by the unexpected intricate structures of radio echoes from the bottom of the Antarctic ice sheet, Nye & Berry [1] conducted ultrasound pulse experiments on a rough surface, allowing them to establish the emergence of singularities in wave trains, *optical vortexes*. These are singular points where the electromagnetic field goes to zero and around which the phase forms an n-armed spiral profile, with n the topological charge (see [2–4] and references therein). In low-order Gauss–Laguerre beams, a single optical vortex corresponds to a phase singularity on the beam axis [5]. Optical vortexes have been introduced on symmetry grounds as the topological defects arising above the laser transition [6] and, in this context, identified as phase singularities appearing and disappearing in pairs of opposite charge. Reported in several experiments, such as photorefractive cavities [7] and lasers [8,9], phase

Royal Society **Publishing**
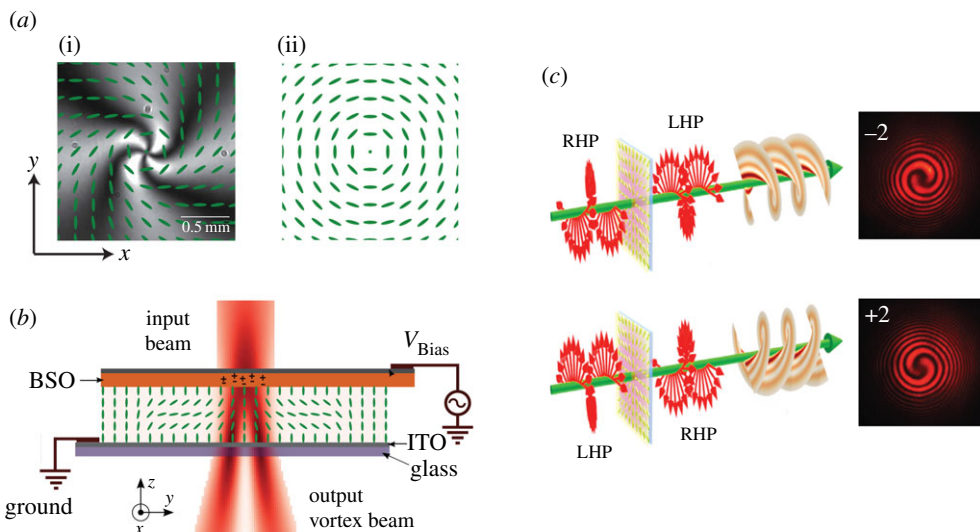
Figure 1. (*a*) Umbilical defect exhibiting swirling arms with superposed molecular organization (i); for comparison the molecular organization of a defect with straight cross arms is shown in (ii). (*b*) Set-up for the optical induction of a matter vortex induction: a circularly polarized beam is incident on the photoconductive side of the LC light valve; the voltage V_{Bias} is such that only the illuminated region undergoes the Fréedericksz transition; when reorienting, the LC molecules follow the circular pattern associated with the electric field and create the matter vortex; this, in turn, induces an optical vortex at the exit of the sample. (*c*) Schematic of the spin–orbital angular momentum transfer through the optically induced defect: an RHP (LHP) circularly polarized beam is converted into an LHP (RHP) beam with a phase singularity of topological charge -2 $(+2)$; experimental interferograms are shown beside the respective panels. (Online version in colour.)

singularities are currently receiving a lot of attention in view of their applications, e.g. light–matter angular momentum exchange [10], optical tweezers [11–13], quantum computation [14], astronomical imaging [15] and data transmission [16].

Optical vortexes have mainly been generated with spiral phase plates [17] or diffractive elements [18]. Recently, the introduction of q-plates, planar elements with a pre-set azimuthal orientation in nematic liquid crystals (LCs), has opened up promising new avenues [19], as well as exploiting the umbilical defects in nematic textures [20]. This approach provides both tunability and high efficiency, although the LC alignment can cause some beam deformation and a consequent degradation of the generated optical vortexes [21]. Recently, by exploiting reorientational nonlinearities in the nematic LC layer of a light valve, we have accomplished the optically addressed self-induction of vortex beams that are self-aligned with the impinging light beam [22]. The spontaneous nature of the induction process guarantees that the generated defect is aligned with the incoming light beam.

In this framework, optical vortexes derive directly from the induced umbilical defects in the LC texture. Indeed, the umbilical defect is one that naturally possesses a vortex-like morphology, making it attractive for spontaneously enabling the matter template to impress a helical structure on an incoming light wavefront. Based on this vortex induction process, we have demonstrated the realization of programmable lattices of optical vortexes with an arbitrary distribution in space [23]. An intriguing property of the induced matter vortexes is their stationary swirling arms (cf. figure 1*a*). These arms are related to the phase jumps of the vortex, or the nullclines (zero-growth isoclines) showed by crossed polarizers, used to characterize the texture of umbilical defects. From the theoretical point of view, this type of behaviour is not usually expected from its universal description, *complex Ginzburg–Landau equation* (CGLE), where the arms are characterized by a cross with straight lines [2].

The aim of this paper is to establish the origin of the swirling arms of the matter vortex trapped by light in a homeotropic nematic LC cell with a photosensitive wall and negative dielectric anisotropy. Based on bifurcation theory, close to the Fréedericksz transition [24], a forced Ginzburg–Landau equation is derived. This equation allows us to understand the origin of the induced vortex, particularly the competition between the forcing generated by the light beam and the elastic medium anisotropy, which generates the swirling of the vortex arms. Numerical simulations of the amplitude equation and experimental observations show quite good agreement.

2. Experimental observation of the optically induced matter vortex

The set-up for vortex induction is sketched in figure 1b. The liquid crystal light valve (LCLV) is prepared by interposing a $d = 15\,\mu m$ layer of nematic LC (MLC6608 from Merck) in between two parallel planar interfaces, a glass plate and a slab of the transparent photoconductor $Bi_{12}SiO_{20}$ (BSO), $25 \times 25\,mm^2$, thickness 1 mm. The interior surfaces are treated to obtain the homeotropic anchoring of the LC, that is, with the nematic director orthogonal to the confining walls (cf. figure 1b). The outer surface of the photoconductor and the inner surface of the glass plate are uniformly coated with thin transparent indium–tin–oxide (ITO) electrodes, through which a voltage V_0 is applied to the cell. The employed LC has a negative dielectric anisotropy, $\epsilon_a = \epsilon_\parallel - \epsilon_\perp < 0$, with $\epsilon_\parallel$ and $\epsilon_\perp$ the dielectric susceptibility for low-frequency electric fields parallel and orthogonal, respectively, to the molecular director [24].

When a bias V_{Bias} is applied to the LCLV beyond the Fréedericskz transition voltage V_{FT}, the molecules tend to reorient perpendicularly to the (low-frequency) electric field because of the negative ϵ_a; hence, since $E = (V_s/d)\hat{z}$ (with V_s the voltage at the LC–BSO interface) is applied along the longitudinal z-direction and the 2π azimuthal degeneracy imposes rotational invariance around it, the LC molecules can arbitrarily align themselves in any direction, spontaneously forming spatial domains separated by umbilical defects or vortexes [24]. In the conducted experiment, we kept $V_{Bias} \lesssim V_{FT}$, in order to avoid spontaneous reorientation while bringing the molecules close to the transition point. When a light beam is incident onto the photosensitive wall of the LCLV, due to the photo-generated charges there is a slight increase in the voltage that effectively drops across the LC region underneath: the Fréedericksz threshold is locally overcome and the molecules start reorienting following the intensity gradients associated with the Gaussian beam profile of the incoming beam. Then, the light on the matter induces, through the photosensitive wall, a vortex with positive topological charge (using the convention of the right-hand rule). Figure 1a illustrates the typically observed vortex when one uses crossed polarizers. The black cross appearing in these conditions is the signature of an umbilical defect, which can be produced by two different types of deformations of the nematic texture, corresponding to ± 1 charge, or winding numbers, of the defect [24].

To prove the optical induction of the matter vortex, and the subsequent transfer from spin to orbital angular momentum, which is mediated by the light–matter interaction, a circularly polarized laser beam of wavelength $\lambda = 632\,nm$, power $P = 0.55\,mW$ is focused to a diameter of $395\,\mu m$ on the photoconductive side of the LCLV. The input beam polarization is taken either right-handed circular or left-handed circular. Typical snapshots of the output beams observed in the two cases are illustrated in figure 2c, where the interferograms, made with a spherical reference wave, show the helical structure of the output wavefront. The bias voltage of the LCLV was fixed to $V_0 = 24\,V$ RMS at frequency 100 Hz. The spin-to-orbital angular momentum transfer is consistent with a $+1$ q-plate; therefore, the matter vortex is a $+1$ defect [19].

A characteristic feature of the observed vortex is that its arms are bent and thus swirling around the defect core. Experimental snapshots showing the matter defect with clockwise and anticlockwise swirling arms are displayed in figure 2a(i) and (ii), respectively. In order to discriminate the sign of the defect, we carried out spatially resolved polarimetry [25]. Using quarter-wave plates, we analysed the local birefringence and reconstructed the director distribution around the defect (figure 2b). The obtained polarimetric profile allowed us to infer

(*a*) (i)   (ii)   (*b*)
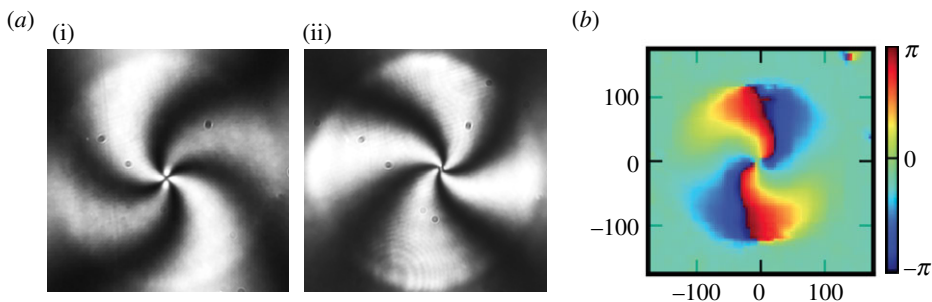
Figure 2. Matter vortex: (*a*) intensity profiles recorded under white light illumination and crossed polarizers showing clockwise (i) and anticlockwise (ii) swirling arms; (*b*) spatially resolved polarimetry in the case of a defect with anticlockwise swirling arms. (Online version in colour.)

that the defect is indeed umbilical and of winding number $+1$. Note that the reconstructed phase is 2θ, with θ the LC tilt in the transverse plane; therefore, the 4π phase jump around the singularity indicates a 2π change of the LC tilt angle θ. In addition, this type of method allows us to observe the bending of the arms of the vortex (cf. figure 2*b*).

3. Amplitude equation close to the Fréedericksz transition

In order to elucidate the mechanism of creation and pinning of matter vortexes, we derive an amplitude equation in the vicinity of the Fréedericksz transition, a limit where analytical results are accessible as nematic LC molecules are weakly tilted from the longitudinal axis $\hat{z}$ and backflow effects can safely be neglected. Illuminating the LCLV with a Gaussian beam induces a voltage drop with a bell-shaped profile across the LC layer, higher in the centre of the illuminated area. To determine the shape of the voltage drop within the sample, one can consider the sample as consisting of two infinitely extended planar parallel plates separated by a distance d. The upper plate, located at $z = d$, is lit by a Gaussian beam. By introducing cylindrical coordinates, the voltage $V(r, \theta, z)$ satisfies the Laplace equation

$$\partial_{zz} V + \frac{\varepsilon_\perp}{\varepsilon_\parallel} \nabla_\perp^2 V = 0,$$

where $\nabla_\perp^2$ stands for the transverse Laplacian operator in polar coordinates. The voltage satisfies the boundary conditions in the respective plates $V(r, \theta, z = d) = V_0 + \alpha I(r)$ and $V(r, \theta, z = 0) = 0$, with V_0 the voltage across the LC layer in the absence of light, (r, θ) the polar coordinates in the plane where the origin of the coordinate system corresponds to the centre of the beam and $\theta = 0$ accounts for the x-axis (figure 1*b*), $I(r)$ stands for the intensity of the Gaussian beam, and $I(r) = I_0 e^{-r^2/\omega^2}$, with I_0 the peak intensity and ω the beam waist. By using the Fourier transform in polar coordinates and solving the above equation with the corresponding boundary conditions, after straightforward calculations one obtains

$$V(z, r) = \frac{1}{2\pi} \int_{-\infty}^{\infty} dk\, e^{-ik \cdot r_\perp} \frac{\sinh\left(\sqrt{\varepsilon_\perp/\varepsilon_\parallel}\, kz\right)}{\sinh(\sqrt{\varepsilon_\perp/\varepsilon_\parallel}\, kd)} \left(\int_0^{\infty} dr_\perp^*\, e^{ik \cdot r_\perp^*} \left[V_0 + \alpha I \left(\frac{r_\perp^*}{\omega} \right) \right] \right).$$

This expression is an exact analytical solution; however it is too intricate to infer results from it. For the sake of simplicity, we consider the limit of a Gaussian beam sufficiently flattened ($\omega \to \infty$). In this limit, the above expression, at the dominant order, takes the form

$$V(z, r) \approx \frac{z}{d} \left[V_0 + \alpha I \left(\frac{r}{\omega} \right) \right].$$

The first and second terms on the right-hand side account for the externally applied bias and the voltage drop induced by the Gaussian beam impinging on the sample, respectively. Figure 3*a*
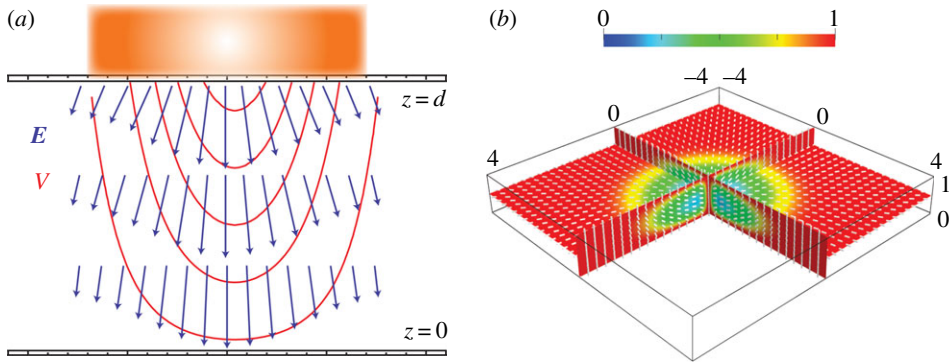
Figure 3. (a) Vertical cross section showing a schematic of the electric field (arrows) and voltage drop (isolines) across the LC layer when a laser beam illuminates the sample from above; (b) corresponding top view of the LC director orientation; the illuminating laser beam is impinging at the centre of the sample. (Online version in colour.)

illustrates the voltage drop inside the LCLV in a vertical cross-sectional view. Then, the electric field $E(r, \theta, z)$ inside the LCLV takes the form

$$E = -\nabla V = E_z \hat{z} + E_r \hat{r} = -\frac{1}{d}\left[V_0 + \alpha I\left(\frac{r}{\omega}\right)\right]\hat{z} - \frac{z\alpha}{d\omega}\frac{\mathrm{d}I(r/\omega)}{\mathrm{d}r}\hat{r},$$

with $\hat{z}$ and $\hat{r}$ the unit vectors in cylindrical coordinates (figure 3a). Note that the electric field contains an axisymmetrical structure. This structure will be responsible for inducing a matter vortex (cf. figure 3). The presence of an inhomogeneous electric field strongly modifies the dynamics of the LC director n. The dynamical equation for the molecular director n reads [26]

$$\gamma \partial_t n = K_3[\nabla^2 n - n(n \cdot \nabla^2 n)] + (K_3 - K_1)[n(n \cdot \nabla)(\nabla \cdot n) - \nabla(n \cdot \nabla)]$$
$$+ 2(K_2 - K_3)[(n \cdot \nabla \times n)(n(n \cdot \nabla \times n) - \nabla \times n) + n \times \nabla(n \cdot \nabla \times n)]$$
$$+ \varepsilon_a(n \cdot E)[E - n(n \cdot E)],$$

where γ is the relaxation time and $\{K_1, K_2, K_3\}$ are the nematic LC elastic constants [24,26]. The dynamical behaviour of the director is of relaxation type and is characterized by preserving its norm. The homeotropic state, $n = \hat{z}$, undergoes a stationary instability for critical values of the voltage $V_0 \equiv V_{\mathrm{FT}} = \sqrt{-K_3\pi^2/\varepsilon_a}$, which corresponds to the Fréedericksz transition of the LC [24,26]. Close to this transition point, and by considering the inhomogeneous electric field $E(r, \theta, z)$, at the dominant order one can use the following ansatz for the amplitude of the critical mode:

$$n(r, \theta, z) \approx \begin{pmatrix} u(r, \theta, t)\sin\left(\dfrac{\pi z}{d}\right) \\ w(r, \theta, t)\sin\left(\dfrac{\pi z}{d}\right) \\ 1 - \dfrac{(u^2 + w^2)}{2}\sin^2\left(\dfrac{\pi z}{d}\right) \end{pmatrix}.$$

Introducing the above ansatz in the director equation, integrating in the z coordinate over one period, and defining the complex amplitude $A \equiv u + iw$, after straightforward calculations one obtains

$$\gamma \partial_t A = \mu A - aA|A|^2 + K\nabla_\perp^2 A + \delta\partial_{\eta,\eta}\bar{A} + b\frac{E_r(z)}{z}E_z\,\mathrm{e}^{i\theta}, \tag{3.1}$$

which is the amplitude equation for self-stabilization of the matter vortex [23]. Here $\mu \equiv -K_3 k^2 - \varepsilon_a E_z^2(r, z)$ is the bifurcation parameter (note that μ is a spatially dependent parameter), $k \equiv \pi/d$, $a \equiv -(K_3 k^2/4 + 3\varepsilon_a E_z^2/4) > 0$ is a parameter of order one that accounts for the nonlinear saturation, $b \equiv \varepsilon_a 2d/\pi$, $\partial_\eta \equiv \partial_x + i\partial_y$, $K \equiv (K_1 + K_2)/2$ and $\delta \equiv (K_1 - K_2)/(K_1 + K_2)$ accounts for the elastic
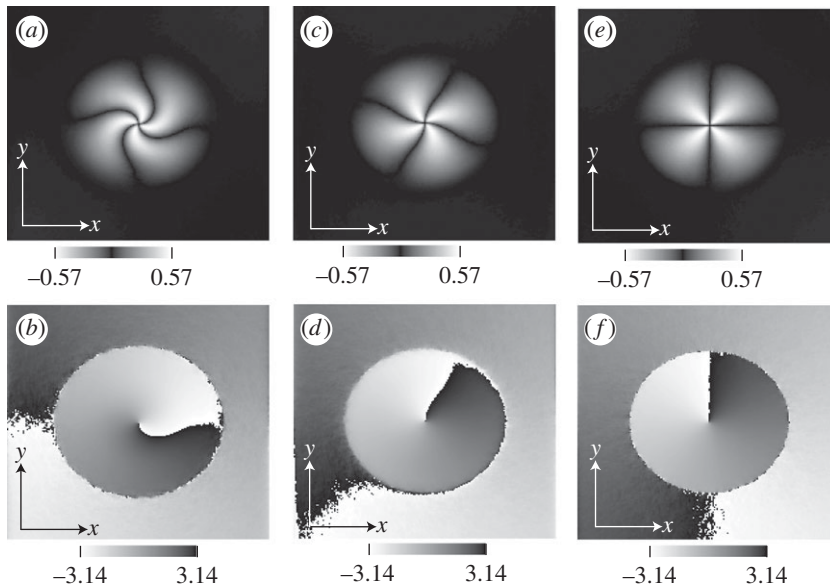
Figure 4. Vortex solution of the anisotropic and forced amplitude equation (3.1) with positive anisotropy ($\delta > 0$) and (a,b) $\theta_0 = 0$, (c,d) $\theta_0 = \pi/4$, and (e,f) $\theta_0 = \pi/2$. The top and bottom panels represent, respectively, the nullcline field $\psi(r,\theta)$, and the phase of the amplitude A. Simulations realized with $\mu = -0.5 + 1.69\,e^{-r^2/\sigma^2}$, $\sigma = 18$, $\delta = 0.7$ and $b(E_r/z)E_z = 0.00169r\,e^{-r^2/\sigma^2}$.

anisotropy. Note that $E_r(z)/z = -(\alpha/d\omega)\,dI(r/\omega)/dr$ does not depend on the z coordinate. In order to elucidate the swirling arms, we consider an extra parameter in the external forcing, changing $E_z\,e^{i\theta}$ for $E_z\,e^{i(\theta+\theta_0)}$.

The last term on the right-hand side is an external forcing generated by the inhomogeneous radial electric field, which in turn is induced by the inhomogeneous profile of the light beam. This forcing term is responsible for inducing a matter vortex with positive charge in the centre position where the applied Gaussian beam is peaked, which is at the origin of the self-stabilization mechanism for the vortex induction.

In order to characterize the dynamics of the arms of the vortex and to allow a direct comparison with the observations obtained by using crossed polarizers, let us introduce the nullcline field $\psi(r,\theta) \equiv \mathrm{Re}(A)\,\mathrm{Im}(A)$. This auxiliary field becomes zero when the real or imaginary part of A vanishes. Then, the arms and position of the vortex are represented, respectively, by the zero and the intersection of the zero nullcline curves. Figure 4 shows the nullcline field and the phase field obtained by using the above Ginzburg–Landau equation with anisotropic forcing, equation (3.1). Note that the vortexes shown in the left and centre panels are similar to those observed experimentally (figure 1). The anisotropic term (the term proportional to δ) is responsible for moving and slightly rotating the matter vortex, as we will see later.

4. Positive vortex with swirling arms

Neglecting anisotropy $\delta = 0$ ($K_1 = K_2 = K_3$) and spatial variations of the voltage ($E_r = 0$), the above model reduces to the well-known CGLE with real coefficients. This model has gathered a great interest by describing various physical systems such as fluids, superfluids, superconductors, LCs, magnetic media and optical cavities, to mention a few [2]. The main properties of the CGLE are reported in a review [27]. The CGLE admits stable dissipative vortex solutions with topological charge (winding number) ± 1 [2]. To characterize these stationary solutions, let us consider the polar representation and polar coordinates $A = R_v(r)\,e^{i(m\theta+\varphi_0)}$, where $m = \pm 1$ is the topological

7

rsta.royalsocietypublishing.org Phil. Trans. R. Soc. A 372: 20140019
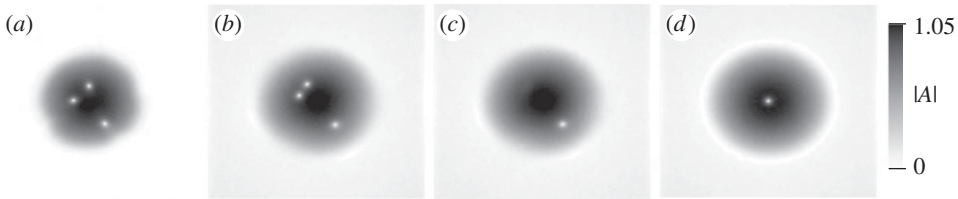
Figure 5. Dynamical evolution of the vortexes observed in the forced amplitude equation (3.1) without anisotropy ($\delta = 0$) starting from the unstable state, $A = 0$, with an initial noise. The temporal evolution is from (a) to (d). The magnitude of the amplitude $|A|$ is displayed in greyscale. The steady state, which corresponds to a single vortex trapped in the centre, is shown in (d). Simulations realized with $\mu = -0.5 + 1.69\,e^{-r^2/\sigma^2}$, $\sigma = 18$, $\delta = 0.7$ and $b(E_r/z)E_z = 0.00169r\,e^{-r^2/\sigma^2}$.

charge, and φ_0 is a continuous parameter that accounts for the phase invariance of the CGLE. The magnitude $R_v(r)$ satisfies

$$\mu_0 R_v - R_v^3 - \frac{m^2}{r^2}R_v + \frac{1}{r}\frac{dR_v}{dr} + \frac{d^2 R_v}{d^2 r} = 0, \qquad (4.1)$$

where $\mu \equiv -K_3 k^2 - \varepsilon_a E_z^2$, measured in the middle of the sample. The defect solution of this model was first observed numerically in [28] and does not have an analytical expression. However, the vortex has the asymptotic behaviour

$$R_v(r) \longrightarrow \begin{cases} r, & r \longrightarrow 0, \\ \sqrt{\mu_0}\left(1 - 2\,e^{-2r\sqrt{\mu_0/2}}\right), & r \longrightarrow \infty. \end{cases} \qquad (4.2)$$

By using Padé approximants, one can obtain suitable approximations for the vortexes [2]. Note that the equation for the modulus of the amplitude (4.1) does not depend on the sign of the topological charge. Hence, the two vortexes are indistinguishable from the point of view of the magnitude. The nullcline field in this case takes the form $\psi(r, \theta) = R_v^2(r) \sin(2\theta)/2$. Thus, the vortex arms are characterized by being straight and orthogonal, forming a cross whose centre determines the position of the vortex. An example of this case is shown in figure 4e. In addition, the phase jump is characterized by a straight line emerging from the position of the vortex (figure 4f).

(a) Effects of forcing

When the Fréedericksz transition starts from the unstable state, $A = 0$, in the presence of noise, or under uniform illumination, the system initially generates a large number of vortexes that subsequently annihilate by pairs of opposite topological charge or fade towards the edges. Let us now consider the effect of forcing, $E_r \neq 0$, occurring in the presence of a non-uniform illumination. Such a forcing simultaneously breaks the translational symmetry and the spatial rotation and, consequently, leads to a single positive vortex to be attracted and trapped in the central position of the addressed area. Figure 5 shows a sequence of pictures illustrating the process described above. Starting from three generated vortexes, a couple of them, oppositely charged, mutually attract and annihilate (figure 5a–c), thus leaving a single positive vortex at the end (figure 5c). The single vortex is then attracted to the centre of the illuminated area where it remains pinned. The stationary pinned vortex is depicted in figure 5d.

Figure 4e and f shows, respectively, the nullcline field and the corresponding phase of the induced stationary vortex. Note that negatively charged vortexes are not consistent with the charge induced by the forcing; thus they are not a steady state. Note also that the phase jump is always consistent with that imposed by the forcing (θ_0).

(b) Effects of elastic anisotropy

We now focus on the effect of elastic anisotropy on the single positive vortex. We first ignore the inhomogeneous forcing; hence, we take $E_r = 0$. In this case, the amplitude of the critical mode satisfies the anisotropic Ginzburg–Landau equation [29]

$$\gamma\, \partial_t A = \mu_0 A - a A |A|^2 + K \nabla_\perp^2 A + \delta \partial_{\eta,\eta} \bar{A}. \tag{4.3}$$

By introducing the ansatz $A(r, \theta) = R(r)\, e^{i(\theta + \varphi_0)}$ in the above equation for the vortex solution with positive topological charge, we obtain the following set of scalar equations:

$$0 = \mu_0 R - a R^3 + (K + \delta\, e^{-2i\varphi_0}) \left(\frac{d^2 R}{d^2 r} + \frac{1}{r} \frac{dR}{dr} - \frac{R}{r^2} \right) \tag{4.4}$$

and

$$0 = \delta \sin 2\varphi_0 \left(\frac{d^2 R}{d^2 r} + \frac{1}{r} \frac{dR}{dr} - \frac{R}{r^2} \right). \tag{4.5}$$

From equation (4.5), the only possibility to obtain a non-trivial solution is to consider the phase parameter satisfying $\sin 2\varphi_0 = 0$, which gives the solutions $\varphi_0 = \{0, \pi/2, \pi, 3\pi/2\}$. Therefore, from the continuous family of possible phase jumps, only four possibilities survive. On the other hand, the equation for the magnitude of the amplitude reads

$$0 = \mu_0 R - a R^3 + (K + \delta \cos 2\varphi_0) \left(\frac{d^2 R}{d^2 r} + \frac{1}{r} \frac{dR}{dr} - \frac{R}{r^2} \right). \tag{4.6}$$

Owing to the periodicity of the cosine function, we only have two possibilities, $\cos 2\varphi_0 = \pm 1$. Rescaling the space by the factor $\sqrt{1 \pm \delta}$, the above equation becomes equation (4.1). Therefore, the isotropic positive vortex has the solution

$$A = R_v \left(\frac{r}{\sqrt{1 \pm \delta}} \right) e^{i(\theta + \pi/4 \mp \pi/4 + n\pi)}, \tag{4.7}$$

with $n = 0, \pm 1, \pm 2, \ldots$. Consequently, the anisotropic vortex solution with positive charge corresponds to a simple scaling of the isotropic vortex solution, notwithstanding, with a finite number of possible phase jumps ($\varphi_0 = \{0, \pi/2, \pi, 3\pi/2\}$), in opposition, with the isotropic system, which has an infinite number of solutions parametrized by the continuous parameter φ_0. Of the four solutions found, those with a smaller core are stable and the others are unstable. It can be inferred from energy calculations, or through numerical simulations, that for positive (negative) anisotropy the stable solutions are $\varphi_0 = \{\pi/2, 3\pi/2\}$ ($\varphi_0 = \{0, \pi\}$). It is worth noting that it is known, from the variational approach to the Frank free energy, that the elastic anisotropy allows a discrete number of four possible phase jumps for umbilical defects [30,31]. These conditions are recovered by the above solutions.

(c) Simultaneous effect of anisotropy and forcing

We now consider simultaneously the effects of the elastic anisotropy, which is intrinsic to the medium properties, and the spatial forcing that is induced by the light. While the forcing induces a vortex that is pinned at the centre of the light beam and tries to impose the phase jump in θ_0, the elastic anisotropy imposes a phase jump that must be consistent with the four above-mentioned φ_0. Because the anisotropy is proportional to the spatial derivatives, we expect it to be more relevant near the core of the vortex. Therefore, one expects that the anisotropy is imposing the phase jump in the region close to the vortex core and the spatial forcing imposes the phase jump in the outer regions of the vortex. Figure 4 illustrates stationary vortexes for positive anisotropy ($\varphi_0 = \{\pi/2, 3\pi/2\}$ are privileged) with different θ_0. In the left, centre and right panels are considered $\theta_0 = 0$, $\theta_0 = \pi/4$ and $\theta_0 = \pi/2$, respectively. As a result of adjusting the respective angles of the phase jump, the vortex solution exhibits a phase gradient, which induces a small force responsible for slightly displacing the vortex from its centre.
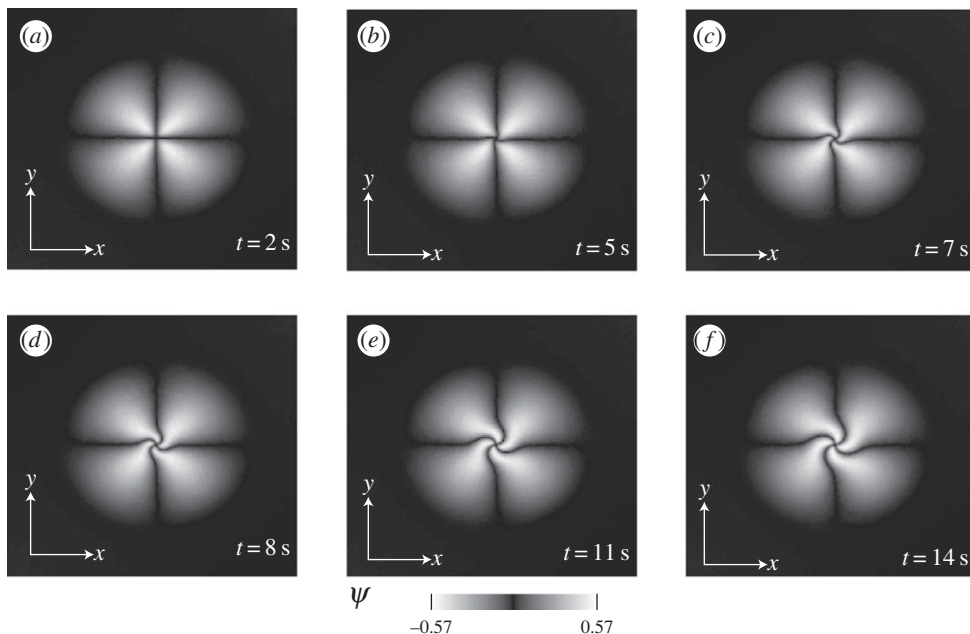
Figure 6. Bending process of the arms of a single positive vortex obtained from the forced amplitude equation (3.1) for positive elastic anisotropy. The time evolution corresponds to (*a*) to (*f*). The nullcline field ψ is displayed in greyscale. During its evolution, the vortex develops a swirling of the arms around its core. The final configuration is shown in (*f*). Simulations realized with $\mu = -0.5 + 1.69\,e^{-r^2/\sigma^2}$, $\sigma = 18$, $\delta = 0.7$, and $b(E_r/z)E_z = 0.00169r\,e^{-r^2/\sigma^2}$; the time shown is scaled by γ.

Therefore, the origin of the bent arms of the vortexes is simply the result of the competition between two effects: the anisotropy, imposing a phase jump angle in the core of the vortex, and the spatial forcing, imposing another phase jump angle in the outside regions. Figure 6 shows the evolution of a positive vortex initially consistent with the spatial forcing and its later temporal evolution resulting from the anisotropy. Clearly, a process of bending of the arms of the vortex is originated from the core. These numerical findings are consistent with the experimental observations.

5. Conclusion and comment

By using a nematic LC in a homeotropic light-valve geometry, we experimentally demonstrated a robust phenomenon of controlled vortex induction, which is, at the same time, spontaneous, self-stabilizing and positionally stable. After its induction, the vortex develops a swirling of the arms, which remain stationary and stable. Close to the Fréedericksz transition, an amplitude equation is derived, which allows us to understand the origin of the induced vortex and the competition between the forcing induced by the light and the elastic anisotropy that generates the swirling arms of the vortex. More precisely, the spatial forcing induces a single charge vortex, then the anisotropy imposes a phase jump in the region close to the vortex core and the spatial forcing imposes a phase jump in the outer regions. Numerical simulations of the amplitude equation show a fairly good agreement with the experimental observations.

Vortexes with swirling arms are usually observed in vortex interactions [32]. They have also been observed in LCs with an active surface [33] and in singular birefringent patterns generated by non-singular light beams [34]. All these observations can be understood as the result of the combination of the elastic anisotropy and an external forcing given, for instance, by another vortex, or by the boundary conditions, or an external field. The anisotropy and the external forcing try to impose the phase jump in different directions, generating a vortex with swirling arms.

By means of appropriate illumination profiles, one could induce vortexes of opposite charges in the same LC sample with a photosensitive wall. The interaction of oppositely charged vortexes exhibits a complex dynamics [2,32]. The characterization of the interaction of vortexes with swirling arms is a work in progress.

References

1. Nye JF, Berry MV. 1974 Dislocations in wave trains. *Proc. R. Soc. Lond. A* **336**, 165–190. (doi:10.1098/rspa.1974.0012)
2. Pismen LM. 1999 *Vortices in nonlinear fields*. New York, NY: Oxford Science Publications.
3. Soskin MS, Vasnetov MV. 2001 Singular optics. In *Progress in optics*, vol. 42 (ed. E Wolf), pp. 219–276. Amsterdam, The Netherlands: Elsevier. (doi:10.1016/S0079-6638(01)80018-4)
4. Staliunas K, Sanchez-Morcillo VJ. 2003 *Transverse patterns in nonlinear optical resonators*. Springer Tracts in Modern Physics, vol. 183. Berlin, Germany: Springer. (doi:10.1007/3-540-36416-1)
5. Yao AM, Padgett MJ. 2011 Orbital angular momentum: origins, behavior and applications. *Adv. Opt. Photonics* **3**, 161–204. (doi:10.1364/AOP.3.000161)
6. Coullet P, Gil L, Rocca F. 1989 Optical vortices. *Opt. Commun.* **73**, 403–408. (doi:10.1016/0030-4018(89)90180-6)
7. Arecchi FT, Giacomelli G, Ramazza PL, Residori S. 1991 Vortices and defect statistics in two-dimensional optical chaos. *Phys. Rev. Lett.* **67**, 3749. (doi:10.1103/PhysRevLett.67.3749)
8. Brambilla M, Battipede F, Lugiato LA, Penna V, Prati F, Tamm C, Weiss CO. 1991 Transverse laser patterns. I. Phase singularity crystals. *Phys. Rev. A* **43**, 5090. (doi:10.1103/PhysRevA.43.5090)
9. Weiss CO, Telle HR, Staliunas K, Brambilla M. 1993 Restless optical vortex. *Phys. Rev. A* **47**, R1616. (doi:10.1103/PhysRevA.47.R1616)
10. Allen L, Beijersbergen MW, Spreeuw RJC, Woerdman JP. 1992 Orbital angular momentum of light and the transformation of Laguerre–Gaussian laser modes. *Phys. Rev. A* **45**, 8185. (doi:10.1103/PhysRevA.45.8185)
11. Grier DG. 2003 A revolution in optical manipulation. *Nature* **424**, 810–816. (doi:10.1038/nature01935)
12. Shvedov VG, Rode AV, Izdebskaya YV, Desyatnikov AS, Krolikowski W, Kivshar YS. 2010 Giant optical manipulation. *Phys. Rev. Lett.* **105**, 118103. (doi:10.1103/PhysRevLett.105.118103)
13. Padgett M, Bowman R. 2011 Tweezers with a twist. *Nat. Photonics* **5**, 343–348. (doi:10.1038/nphoton.2011.81)
14. Arnaut HH, Barbosa GA. 2000 Orbital and intrinsic angular momentum of single photons and entangled pairs of photons generated by parametric down-conversion. *Phys. Rev. Lett.* **85**, 286–289. (doi:10.1103/PhysRevLett.85.286)
15. Tamburini F, Anzolin G, Umbriaco G, Bianchini A, Barbieri C. 2006 Overcoming the Rayleigh criterion limit with optical vortices. *Phys. Rev. Lett.* **97**, 163903. (doi:10.1103/PhysRevLett.97.163903)
16. Wang J *et al.* 2012 Terabit free-space data transmission employing orbital angular momentum multiplexing. *Nat. Photonics* **6**, 488–496. (doi:10.1038/nphoton.2012.138)
17. Beijersbergen MW, Allen L, van der Veen HELO, Woerdman JP. 1993 Astigmatic laser mode converters and transfer of orbital angular momentum. *Opt. Commun.* **96**, 123–132. (doi:10.1016/0030-4018(93)90535-D)
18. Sacks Z, Rozas D, Swartzlander GA. 1998 Holographic formation of optical-vortex filaments. *J. Opt. Soc. Am.* **B15**, 2226–2234. (doi:10.1364/JOSAB.15.002226)
19. Marrucci L, Manzo C, Paparo D. 2006 Optical spin-to-orbital angular momentum conversion in inhomogeneous anisotropic media. *Phys. Rev. Lett.* **96**, 163905. (doi:10.1103/PhysRevLett.96.163905)
20. Brasselet E. 2012 Tunable optical vortex arrays from a single nematic topological defect. *Phys. Rev. Lett.* **108**, 087801. (doi:10.1103/PhysRevLett.108.087801)

21. Bekshaev AY, Sviridova SV. 2010 Effects of misalignments in the optical vortex transformation performed by holograms with embedded phase singularity. *Opt. Commun.* **283**, 4866–4876. (doi:10.1016/j.optcom.2010.07.031)

22. Barboza R, Bortolozzo U, Assanto G, Vidal-Henriquez E, Clerc MG, Residori S. 2012 Vortex induction via anisotropy stabilized light–matter interaction. *Phys. Rev. Lett.* **109**, 143901. (doi:10.1103/PhysRevLett.109.143901)

23. Barboza R, Bortolozzo U, Assanto G, Vidal-Henriquez E, Clerc MG, Residori S. 2013 Harnessing optical vortex lattices in nematic liquid crystals. *Phys. Rev. Lett.* **111**, 93902. (doi:10.1103/PhysRevLett.111.093902)

24. Chandrasekhar S. 1977 *Liquid crystals*. New York, NY: Cambridge University Press.

25. Soskin MS, Denisenko VG, Egorov RI. 2004 Singular Stokes-polarimetry as new technique for metrology and inspection of polarized speckle fields. *Proc. SPIE* **5458**, 79. (doi:10.1117/12.544681)

26. de Gennes PG, Prost J. 1993 *The physics of liquid crystals*, 2nd edn. New York, NY: Oxford Science Publications.

27. Aranson I, Kramer L. 2002 The world of the complex Ginzburg–Landau equation. *Rev. Mod. Phys.* **74**, 99–143. (doi:10.1103/RevModPhys.74.99)

28. Ginzburg VL, Pitaeskii LP. 1958 On the theory of superfluidity. *Sov. Phys. JETP* **7**, 858.

29. Frisch T, Rica S, Coullet P, Gilli JM. 1994 Spiral waves in liquid crystal. *Phys. Rev. Lett.* **72**, 1471–1474. (doi:10.1103/PhysRevLett.72.1471)

30. Rapini A. 1973 Umbilics: static properties and shear-induced displacements. *J Physique* **34**, 629–633. (doi:10.1051/jphys:01973003407062900)

31. Nehring JR, Saupe A. 1972 On the schlieren texture in nematic and smectic liquid crystals. *J. Chem. Soc.* **2**, 1–15. (doi:10.1039/f29726800001)

32. Barboza R, Sauma T, Bortolozzo U, Assanto G, Clerc MG, Residori S. 2013 Characterization of the vortex-pair interaction law and nonlinear mobility effects. *New J. Phys.* **15**, 013028. (doi:10.1088/1367-2630/15/1/013028)

33. McCamley MK, Crawford GP, Ravnik M, Žumer S, Artenstein AW, Opal SM. 2007 Optical detection of anchoring at free and fluid surfaces using a nematic liquid crystal sensor. *Appl. Phys. Lett.* **91**, 141916. (doi:10.1063/1.2795347)

34. Brasselet E. 2009 Singular optical manipulation of birefringent elastic media using nonsingular beams. *Opt. Lett.* **34**, 3229–3231. (doi:10.1364/OL.34.003229)